

Comprehensive strain analysis in thin films based on high-resolution x-ray diffraction: Application to implanted LiNbO_3

D. Shilo, E. Lakin, and E. Zolotoyabko

Department of Materials Engineering, Technion—Israel Institute of Technology, Haifa 32000, Israel

(Received 4 August 2000; published 3 May 2001)

Strain analysis of thin film heterostructures is expanded to noncubic crystalline symmetries with special attention to the practically important hexagonal and rhombohedral systems. The developed formalism is rather general and can be used to study systems with highly anisotropic lattice mismatches (even unknown) and strain degrees. It is applied here to analyze complex structural modifications in the near-surface waveguide layers produced by He-implantation in Y -cut LiNbO_3 wafers, which initially have the rhombohedral Bravais lattice. Experimental results, obtained by x-ray mapping of reciprocal space in the vicinity of symmetric and asymmetric reflections, showed a strong anisotropy of the layer-lattice mismatch in plane perpendicular to the three-fold axis. This result unequivocally indicates that the initial rhombohedral symmetry of the unit cell is broken as a result of ion implantation. Experimental findings are explained in terms of strain-induced ordering of point defects, which is a well-known phenomenon in the field of physical metallurgy, but has never been mentioned in the studies of thin film structures for microelectronics and optoelectronics. Since this phenomenon can be important to other layered structures, it is included into a general solution of the elasticity problem.

DOI: 10.1103/PhysRevB.63.205420

PACS number(s): 61.10.Nz, 81.40.Jj, 68.55.Ln, 42.79.Gn

I. INTRODUCTION

Modern microelectronic and optoelectronic devices are built on strained thin film heterostructures.¹ The lattice strain can appear during epitaxial growth of differently composed layers or as a result of device processing, such as ion implantation, thermal treatment, oxidation, etc. Precise data on strain levels have crucial importance to device functioning, since lattice strain strongly affects such film characteristics as band-gap energy, carrier mobility, dielectric tensor, and refractive index.

Strain field in thin films is determined by the spatial distribution of lattice parameters and, in principle, can be deduced from high-resolution x-ray diffraction measurements. In order to relate the measured lattice parameter variations to strain values, an elasticity problem should be solved, which takes proper account of crystal symmetry. General solution provides the relationship between the measured lattice parameter changes; the structural characteristics, such as lattice mismatches (and, hence, the epilayer composition); and the strain degrees that can be expressed via misfit dislocation densities.

An elasticity problem for a heterostructure, composed of a cubic film epitaxially deposited on a cubic substrate of arbitrary orientation, had been solved in Refs. 2–4. They obtained solutions that are based on an assumption that the in-plane strain field (i.e., that is confined in the plane of film/substrate interface) is isotropic. Two conditions must be fulfilled in order to validate this assumption.

- (1) Densities of misfit dislocations along the coordinate axes in the interface plane should be equal.
- (2) In-plane lattice mismatch should be isotropic.

However, experimental results^{5–8} show that in some Si and zinc-blende-based structures the misfit dislocation densities differ when measuring along $[110]$ and $[1\bar{1}0]$ directions. Hence, strictly speaking, the existing solution for cubic

heterostructures is only valid in fully strained situations with no misfit dislocations.

In recent years there has been a growing interest to implement noncubic (mainly hexagonal and rhombohedral) single crystals, such as GaN, AlN, SiC, Al_2O_3 , LiNbO_3 , etc., into modern device technology. Reduction of the unit cell symmetry makes strain analysis much more complicated. If the crystal symmetry differs from the cubic one, the lattice mismatch is no longer isotropic. For example, in a hexagonal lattice, which will be considered below, a mismatch in the Z direction (six-fold axis) is different from that in the X and Y directions. If the Z axis is situated in the interface plane, the in-plane lattice mismatch will be anisotropic. However, in many cases the components of lattice mismatch continue to follow the Vegard rule, i.e., they are proportional to the layer composition (although the proportionality factor may be different for the X , Y , and Z directions), and, hence, are determined by a single parameter: atomic concentration.^{9,10} For such structures a solution, given in Ref. 2, has been generalized in Ref. 11 in order to describe lattice strains in crystals with reduced symmetry. However, this solution only remains valid for fully strained structures.

In Sec. II of this paper a general approach to solve the elasticity problem is developed that can be applied to any crystalline system. This approach is free from the strain isotropy assumption and, hence, it can be applied to partially relaxed layered structures as well. Moreover, the proposed analysis can be used in complicated situations when an initial lattice mismatch is unknown or the Vegard rule is not valid. A good example is a heterostructure fabricated by ion implantation. The latter leads to the modification of lattice parameters due to implantation-induced lattice damage. As is shown below, such rather heavy treatment can even result in the breaking of initial crystal symmetry, that should be taken into account when analyzing experimental data.

Abilities of the developed formalism are illustrated by experimental results obtained with He-implanted and an-

nealed LiNbO₃ single crystals, having initial rhombohedral symmetry (which often is represented in the hexagonal setting). Implantation and subsequent heat treatments are used to fabricate waveguide layers for light propagation in LiNbO₃-based optoelectronic devices.¹² Structural modifications in the waveguide layer directly affect the refractive index via electron density changes and strain-induced photoelastic effect. It has been shown that the depth dependence of the changes of refractive index is similar to that of the implantation damage,¹³ and to the variation of the interplanar d -spacing along the ion trajectory.¹⁴ Nevertheless, we are still far from a complete understanding of atomic mechanisms that are responsible for modified optical characteristics.

In order to carry out a comprehensive strain analysis in the LiNbO₃ waveguide layers, the changes of lattice parameters were precisely measured by using x-ray mapping in reciprocal space. Experimental data are displayed in Sec. III.

The obtained results are analyzed in Sec. IV. We show how equations derived in Sec. II can be used to deduce the components of lattice mismatches and strain degrees from measured changes of lattice parameters. Comparison between different components of lattice mismatch allowed us to conclude that the initial rhombohedral symmetry is broken as a result of ion implantation. The driving force of this breakdown is the strain-induced ordering of point defects in an implanted layer. Analysis of experimental data taken from the annealed samples gave straightforward indication that heat treatment at elevated temperatures leads to lattice recovery (via annihilation and migration of postimplantation point defects) rather than to the misfit dislocation formation.

II. THEORETICAL ANALYSIS

A general solution of the elasticity problem in layered structures results in complex expressions that are difficult to analyze and to adopt to real situations. On the other hand, most of the potentially used heterostructures have specific lattice symmetry and orientation that greatly simplify theoretical analysis. Keeping this in mind, we introduce here a general routine for the solution of the elasticity problem (which can be applied to the arbitrary lattice symmetry and orientation) without developing the explicit general expressions.

Instead, the important steps are explained that have to be performed to solve the elasticity problem. Following these steps, the reader will be able to derive explicit expressions for layered structures of particular symmetry. In this paper a complete set of equations is derived for the rhombohedral Y -oriented LiNbO₃ layers, in which anisotropic lattice mismatch (unknown) is introduced by ion implantation. Taking this sufficiently complicated situation as an example, we show a way in which the detailed strain analysis can be carried out.

A. Definitions

Let us consider a single-crystalline thin film that is grown or fabricated on the top of a substrate having the same lattice symmetry and orientation, but slightly different lattice parameters.

The lattice mismatch describes the differences between respective lattice parameters of the substrate and the layer, in its hypothetical free-standing state. Generally, the lattice mismatch is given by a second-rank tensor m_{ij} whose diagonal components

$$m_{ii} = \frac{a_{R,i} - a_{S,i}}{a_{R,i}} \quad (1)$$

are equal to the relative differences in lattice constants along the i axis ($i=X,Y,Z$) of the substrate $a_{S,i}$ and the relaxed film $a_{R,i}$, respectively.

The further analysis is formally valid for systems in which $m_{ii} \ll 1$. Most of the thin film structures satisfy this criterion.

The mismatch tensor m_{ij} has a diagonal form in all crystal classes in which angles between the Bravais lattice vectors are fixed by symmetry constraints. Nondiagonal (shear) components appear only in the monoclinic and triclinic classes in which one or three angles, respectively, are independent lattice parameters. In these cases, the nondiagonal components are defined as the differences between corresponding angles in the substrate and the free-standing layer.

The number of essential mismatch components depends on the crystal symmetry. For example, in cubic crystals there is only one such mismatch since the m_{ij} tensor is diagonal and $m_{xx} = m_{yy} = m_{zz}$.

In general, the lattice parameter differences between the substrate and the layer, which are measured by x-ray diffraction, differ from the mismatches m_{ij} due to the elastic strains in the layer that are produced by the forces acting at the layer/substrate interface. The lattice parameter differences are completely described by the second-rank tensor ξ_{ij} ,

$$\xi_{ij} = \frac{\partial u_i}{\partial x_j}, \quad (2)$$

which is common in the theory of elasticity¹⁵ and is defined via the deformation vector \mathbf{u} that describes the displacements of the layer's atoms from their hypothetical positions according to the order of the substrate's lattice.

Another definition that is often used in thin film studies,¹⁶

$$\xi_{ii} = \frac{a_{L,i} - a_{S,i}}{a_{S,i}}, \quad (3)$$

is based on the comparison between the actual lattice constants of the layer $a_{L,i}$ and the substrate, $a_{S,i}$, along the i axis. Note, that Eq. (3) defines only diagonal elements of the tensor ξ_{ij} . So, in order to take into account the shear strains in the layer, Eq. (2) should generally be used. It is also worthwhile to emphasize that the origin of the shear deformation is not necessarily the "intrinsically" nondiagonal mismatch components (as in monoclinic or triclinic crystals). As will be shown in Sec. IID, shear strains can appear if there are nonzero components of the stiffness tensor that connect between in-plane axial stresses and shear strains.

The difference between the free-standing lattice (described by tensor m_{ij}) and the strained lattice of the layer (described by tensor ξ_{ij}) is defined via the equation:

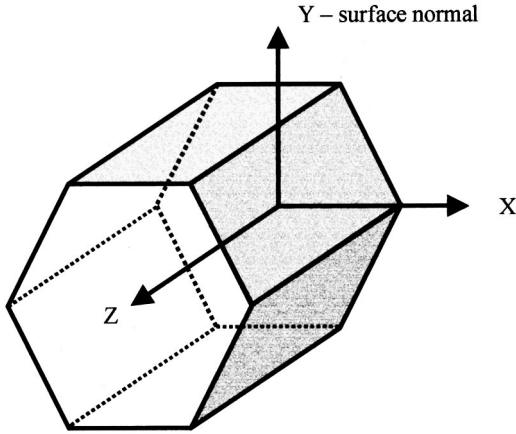


FIG. 1. Unit cell of LiNbO_3 (in hexagonal setting) and a suitable choice of Cartesian coordinate system (X, Y, Z) within it.

$$\xi_{ij} = m_{ij} + e_{ij}. \quad (4)$$

In general case, the tensor e_{ij} is not symmetric and can be divided into a symmetric part ε_{ij} ,

$$\varepsilon_{ij} = (e_{ij} + e_{ji})/2, \quad (5)$$

which describes lattice strains, and an antisymmetric part ω_{ij} ,

$$\omega_{ij} = (e_{ij} - e_{ji})/2, \quad (6)$$

which describes lattice rotations. Substituting Eqs. (1), (3), and (4) into Eq. (5) and neglecting second-order terms of m_{ii} and ξ_{ii} [i.e., replacing $a_{S,i}$ by $a_{R,i}$ in the denominator of Eq. (3)] yields the well-known definition of the diagonal strain components:

$$\varepsilon_{ii} = \frac{a_{L,i} - a_{R,i}}{a_{R,i}}. \quad (7)$$

Before starting to solve the elasticity problem, attention should be paid to an appropriate choice of the coordinate system. It is suitable to choose a coordinate system with two axes located in the plane of the layer/substrate interface and the third axis being perpendicular to it. In order to be able to use Eqs. (1), (3), and (7), the coordinate axes should be some linear combinations of the translation vectors, but it is not obligatory that they coincide with the basis of Bravais lattice. It is much easier to operate with strain tensor components in the orthogonal coordinate system, which is a natural choice for cubic, tetragonal, and orthorhombic crystalline systems. In the cases of rhombohedral and hexagonal symmetry, which are of main interest here, the suitable orthogonal coordinate system is depicted in Fig. 1. In this system, the Z axis coincides with the three-fold or six-fold axis, the X axis is parallel to the triangle or hexagon side, and the Y axis is perpendicular to both the Z and X axes. This coordinate system is also routinely used to describe elastic properties of hexagonal and rhombohedral crystals.¹⁷

Tensor m_{ij} , describing the mismatch between lattice parameters of the layer and the substrate, both of hexagonal or rhombohedral symmetry, does not contain the nondiagonal

terms. Moreover, two of the three diagonal components m_{xx} , m_{yy} , and m_{zz} are equal, viz., $m_{xx} = m_{yy}$, owing to the trigonal symmetry of translation vectors in the XY plane. However, ion implantation produces unpredictable structural changes in the near surface layer due to formation of a large amount of point defects. Under implantation conditions not only are the mismatch values unknown, but also the relations between the mismatch components. It is even possible that the implantation procedure leads to the breakdown of the initial symmetry of the layer, and further analysis of experimental data gives us evidence that this is the case.

B. In-plane strains and misfit dislocations

Interatomic forces, acting on the layer/substrate interface, compel the layer's atoms to fit into the in-plane arrangement of the substrate lattice. Since the layer thickness is much smaller than that of the substrate, one can neglect the substrate strains. For very thin films with the thickness less than some critical value, the system energy is minimized if the interface is fully coherent and the layer is fully strained. This means that the in-plane lattice parameters of the layer, $a_{L,\parallel}$, exactly match those of the substrate, $a_{S,\parallel}$, and, hence, $\xi_{ii} = 0$ for both coordinate axes located in the interface plane.

For thicker layers there is a thermodynamically dictated driving force to form misfit dislocations in order to accommodate lattice mismatch and to diminish elastic strain energy. Despite the dislocation-strain field being nonuniform, it is possible to define effective (or averaged) lattice parameters, which can be put into Eqs. (3) and (7), instead of $a_{L,i}$. This simplification is good enough for layered structures with low dislocation densities, when dislocation-induced modification of lattice parameters is small, $\Delta a/a \ll 1$.

In this case, the effective in-plane lattice parameters of the layer are related to the linear misfit dislocation densities n_i as follows:¹⁸

$$a_{L,i} = a_{S,i}(1 \pm n_i b_i), \quad (8)$$

where b_i is the component of Burgers vector along the i axis. The sign $[+]$ in Eq. (8) corresponds to $a_{R,i} > a_{S,i}$, while the sign $[-]$ corresponds to $a_{R,i} < a_{S,i}$.

Substituting Eq. (8) into Eqs. (3) and (7), yields the following expressions for the in-plane components of tensors ξ_{ij} and ε_{ij} :

$$\xi_{ii} = \pm n_i b_i, \quad (9)$$

$$\varepsilon_{ii} = -m_{ii} \pm n_i b_i. \quad (10)$$

In Eq. (10) we again neglected second-order terms of m_{ii} and ξ_{ii} since $m_{ii} \ll 1$ and $\xi_{ii} \ll 1$.

Another way to describe the effect of misfit dislocation formation consists of the introduction of the strain degree, $0 \leq S_i \leq 1$, which characterizes the strain relaxation processes (see, e.g., Ref. 19). Since the misfit dislocation density n_i is generally anisotropic, the strain degree S_i should also be defined separately for each of two in-plane coordinate axes via the following expression:

$$\varepsilon_{ii} = -m_{ii} S_i. \quad (11)$$

Setting Eq. (10) equal to Eq. (11), gives the relation between the strain degrees and the misfit dislocation densities:

$$S_i = 1 - |n_i b_i| / m_{ii}, \quad (12)$$

where $m_{ii} \neq 0$. Substituting Eq. (12) into Eq. (9) yields

$$\xi_{ii} = m_{ii}(1 - S_i) \quad (13)$$

for two i axes, which are located in the interface plane.

In fully strained state $S_i = 1$, and the misfit dislocation density is $n_i = 0$. Thus, the in-plane strains reach the maximum value of $\varepsilon_{ii} = -m_{ii}$, and the in-plane lattice parameters of the layer match those of the substrate, i.e., $\xi_{ii} = 0$. In the fully relaxed state $S_i = 0$, and the misfit dislocation density reaches the maximum value of $n_i^{\max} = |m_{ii}|/b_i$. At the same time the in-plane strains equal $\varepsilon_{ii} = 0$, and the in-plane lattice parameters of the layer reach their relaxed values, i.e., $a_{L,i} = a_{R,i}$ and $\xi_{ii} = m_{ii}$.

In further analysis we will take into account the possible formation of the misfit dislocations via strain degree parameters [Eqs. (11)–(13)]. In this description the relations between intrinsic lattice characteristics (m_{ii} and S_i) and the two axial strain components along the in-plane axes are given by Eq. (11). As was already mentioned, the in-plane shear component only appears in the monoclinic and triclinic systems. Thus, in our case of the Y -cut LiNbO_3 crystals,

$$\varepsilon_{xx} = -m_{xx}S_x, \quad \varepsilon_{zz} = -m_{zz}S_z, \quad \varepsilon_{xz} = 0. \quad (14)$$

The situation is more complex in the monoclinic and triclinic crystals, especially because of an influence of misfit dislocations on the in-plane shear strain components.

C. Plane stress assumption

The boundary conditions, which should be imposed solving the elasticity problem for a layered structure, assume that there are no forces acting on a free surface of the layer in the perpendicular direction.

Because the layer thickness is a few orders of magnitude less than its lateral dimensions, it is reasonable to assume that the layer stresses act only in the interface plane. This assumption provides the three stress components σ_{ij} with at least one of the indices indicating the normal to the interface, equal to zero.

For the Y -cut LiNbO_3 this assumption yields

$$\sigma_{yy} = \sigma_{xy} = \sigma_{zy} = 0. \quad (15)$$

D. Strain tensor

The three strain components acting in the interface plane have already been found in Sec. II B [see Eq. (14)]. Using plane-stress assumption [Eq. (15)] and Hooke's law, $\sigma_{ij} = C_{ijkl}\varepsilon_{kl}$ (where C_{ijkl} is the stiffness tensor for a given point-group symmetry) yields three equations for the other three strain components ε_{ij} with at least one of the indexes indicating the normal to the interface. For the rhombohedral Y -cut LiNbO_3 crystals (point group $3m$), this procedure yields

TABLE I. LiNbO_3 stiffness constants (GPa), taken from Ref. 20.

C_{11}	C_{12}	C_{13}	C_{14}	C_{33}	C_{44}
203	55	75	8.8	244	60

$$\begin{aligned} \varepsilon_{yy} &= -\frac{(C_{44}C_{12} + C_{14}^2)\varepsilon_{xx} + C_{44}C_{13}\varepsilon_{zz}}{C_{44}C_{11} - C_{14}^2}, \\ \varepsilon_{yz} &= -C_{14}\frac{(C_{11} + C_{12})\varepsilon_{xx} + C_{13}\varepsilon_{zz}}{C_{44}C_{11} - C_{14}^2}, \\ \varepsilon_{xy} &= 0. \end{aligned} \quad (16)$$

In Eq. (16) the standard form of the elastic stiffness tensor with reduced indices (from 4 to 2) is used. The nonzero stiffness constants²⁰ of LiNbO_3 crystals are given in Table I.

The shear strain ε_{yz} appears in Eq. (16) due to the presence of C_{14} component in the stiffness tensor. This is a typical situation for lattices with low symmetry or when the normal to the interface does not coincide with the symmetry axis.²¹ As will be shown in the following sections, the measurement of shear strain is very important to the comprehensive strain analysis.

Note that setting $C_{14} = 0$, $C_{12} = C_{13}$, and $\varepsilon_{xx} = \varepsilon_{zz}$ in Eq. (16) yields the well-known results for cubic crystals:

$$\varepsilon_{yy} = -2(C_{12}/C_{11})\varepsilon_{xx} \quad \text{and} \quad \varepsilon_{yz} = 0. \quad (17)$$

Finally, the substitution of Eq. (14) into Eq. (16) enables us to express all the components of the strain tensor as a function of m_{ij} and S_i .

E. Relationship between the intrinsic lattice characteristics m_{ij} and S_i , and the measured lattice parameter changes ξ_{ij}

The strain state of the layer will be completely defined if the intrinsic lattice characteristics, such as lattice mismatches m_{ij} and strain degrees S_i , are known. However, the quantities measured by means of x-ray diffraction are the lattice parameter changes ξ_{ij} . In order to find the relationship required, let us substitute Eqs. (5) and (6) into Eq. (4). This yields

$$\xi_{ij} = m_{ij} + \varepsilon_{ij} + \omega_{ij}. \quad (18)$$

The only term in Eq. (18) which still has not been expressed via m_{ij} and S_i , is the antisymmetric lattice rotation tensor ω_{ij} . As was explained in Sec. II A, it contributes to the nondiagonal components of tensor ξ_{ij} .

Tensor ω_{ij} may appear due to the tendency to form a coherent interface. Analysis of shear strains in LiNbO_3 layers shows that the coherent interface results in the deformation of a type $\xi_{zy} = 2\varepsilon_{yz}$, while $\xi_{yz} = 0$ (see Fig. 2). Misfit dislocations at the substrate/layer interface can also contribute to the rotation tensor and change the situation schematically illustrated in Fig. 2.

The rotation tensor components can be determined by measuring two nondiagonal terms ξ_{ij} and ξ_{ji} :

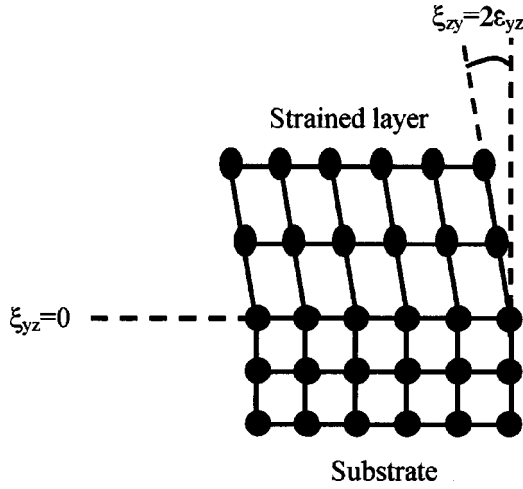


FIG. 2. Schematic illustration of shear deformation in fully strained Y-cut LiNbO₃.

$$\omega_{ij} = (\xi_{ij} - \xi_{ji})/2. \quad (19)$$

Using Eq. (19), the measured values of ω_{ij} can be substituted into Eq. (18) in order to obtain a final relationship between the intrinsic lattice characteristics, m_{ij} and S_i , and the measured lattice parameter changes ξ_{ij} .

In case of the Y-cut LiNbO₃, Eqs. (14), (16), and (18), together with numerical values of elastic stiffness coefficients (see Table I), finally yield

$$\xi_{xx} = m_{xx}(1 - S_x), \quad (20)$$

$$\xi_{yy} = 0.279m_{xx}S_x + m_{yy} + 0.372m_{zz}S_z,$$

$$\xi_{zz} = m_{zz}(1 - S_z),$$

$$2\varepsilon_{yz} = \xi_{zy} + \xi_{yz} = 0.375m_{xx}S_x + 0.109m_{zz}S_z.$$

Thus, we have four equations (according to four measurable lattice parameter changes) that connect five variables: three mismatch parameters and two strain degrees. The system of Eqs. (20) permits an interval of structural parameters, which can be extracted from the experimental data, rather than the unique solution. This is a typical situation in the strain analysis of heterostructures, which is not frequently mentioned in the research reports. Instead, some additional assumptions based on the Vegard rule or on the allegedly known crystal symmetry of strained layer are used, which allow us to avoid the uncertainty mentioned. These assumptions are often considered as self-evident without careful testing of their compatibility to experimental data.

In case of the Y-cut LiNbO₃, an excessive degree of freedom can be removed by assuming $m_{xx} = m_{yy}$, that reflects an initial rhombohedral symmetry. However, it cannot be done *a priori*. By using Eq. (20), one can compose a difference, $A = (m_{yy} - m_{xx})$, as a function of the measured lattice parameter changes:

$$m_{yy} - m_{xx} = A = \xi_{yy} - \xi_{xx} - 3.454(2\varepsilon_{yz}). \quad (21)$$

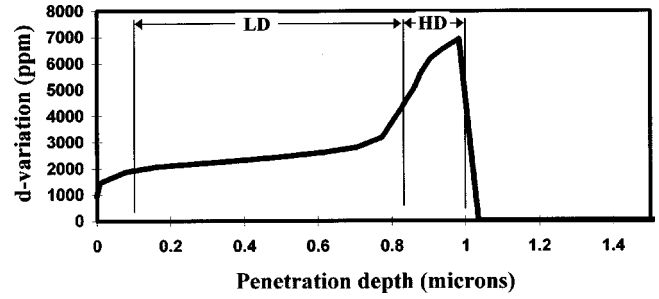


FIG. 3. Typical changes of the out-of-plane (030) d -spacing in as-implanted Y-cut LiNbO₃, as a function of the crystal depth. The separation to ‘‘low damage layer’’ (LD) and ‘‘high damage layer’’ (HD) is indicated.

Equation (21) provides a straightforward way to check an equality, $m_{yy} = m_{xx}$, on the basis of measured data and, if it turns out that $A \neq 0$, to detect possible symmetry breaking induced by ion implantation or other reasons.

III. EXPERIMENT

Y-cut LiNbO₃ wafers, 3 in. in diameter, 0.5 mm thick, with one polished face, were subjected to He implantation in order to produce waveguide layers near the wafer surface. He-ions, of an energy of 320 keV, were implanted at room temperature through the polished face of the wafers at a dose of 2×10^{16} ions/cm². After implantation a part of the samples were subjected to 30-min heat treatments in a furnace under a flow of forming gas, at temperatures ranging between 200 and 470 °C in order to anneal the implantation damage. Structural modifications were measured by high-resolution x-ray diffraction (HRXRD).

In the previous study¹⁴ the HRXRD profiles were taken in the vicinity of the symmetric (030) LiNbO₃ reflection, providing diffraction intensity from atomic planes parallel to the crystal surface. Based on successful fittings between measured and simulated diffraction profiles, the out-of-plane (normal to the surface) changes of the interplanar (030) d -spacing $\Delta d/d$ as a function of crystal depth y were deduced. These dependences (see typical example in Fig. 3) showed that in the first approximation the damaged region, which for the given He-ion energy spans up to 1 μm in depth, consists of two distinct layers. The first layer, which we will call the ‘‘low-damage layer’’ (LD), is situated between 0.1 and 0.85 μm beneath the surface. Within this layer the energy losses dE/dy and the respective implantation damage are moderate and weakly y dependent because of the relatively high velocity of implanted species. Correspondingly, the $\Delta d/d(y)$ function is nearly constant here.

The second layer is confined between 0.85 and 1 μm in depth and is characterized by sharp $\Delta d/d$ variation. At this point the ion velocity is close to zero, and the implanted species are effectively stopped by the nuclear stopping mechanism, producing a large amount of point defects. We will call this layer the ‘‘high-damage layer’’ (HD). Due to the lattice swelling in this layer the electron density and, correspondingly, the refractive index are reduced and, hence, an optical barrier to light propagation into the crystal bulk is

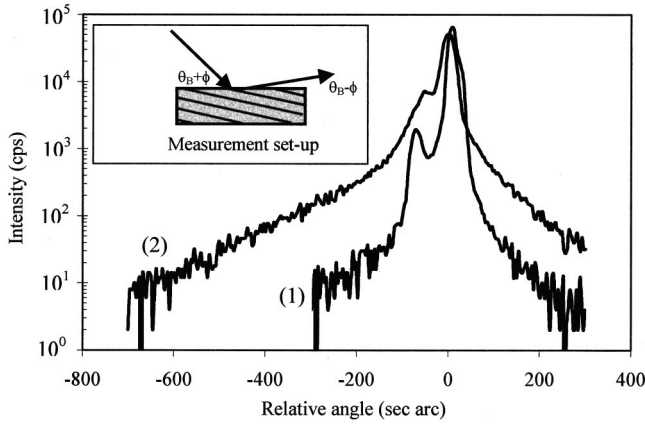


FIG. 4. (220)LiNbO₃ diffraction profiles taken from an as-implanted sample (1) as well as from the sample implanted and annealed at 250 °C (2). Inset shows the scattering geometry for asymmetric reflection.

created.¹⁴ The presence of the optical barrier leads to light confinement near the crystal surface, i.e., provides waveguide properties.

Beyond the HD layer, a nondamaged crystal region (“substrate”) is located, since implanted species do not penetrate there. Implantation-induced lattice mismatch (unknown) at the HD/substrate interface is a driving force for lattice strains there, which can produce additional changes in refractive index via photoelastic effect. Thus, the comprehensive analysis of this complicated problem requires all components of strain tensor to be measured by HRXRD. The measurement procedures are described in the next sections.

A. HRXRD technique

HRXRD is based on the measurements of diffraction profiles in the close vicinity of the Bragg angle θ_B , and on subsequent fittings of the measured intensity distributions to those simulated by means of the dynamical diffraction theory^{22,23} or in the framework of the extended kinematical approach.²⁴ In fact, the latter is well suited for implantation and diffusion problems in thin films.^{25,26} As a result of this fitting, the depth-resolved changes in lattice parameters are extracted, providing information that is unattainable by any other technique.

In case of spatially well-defined layers it is possible to stay within the more simple routine, viz, measuring an angular distance $\Delta\omega$ between diffraction peaks originated in the layer and in the substrate²¹ (see Fig. 4). Angular distance $\Delta\omega$ can be split into two components, $\Delta\theta$ and $\Delta\phi$. The first contribution $\Delta\theta$ appears due to the difference between lattice d spacings d in the layer and in the substrate:

$$\Delta\theta = -\tan\theta_B \frac{\Delta d}{d}. \quad (22)$$

The second term $\Delta\phi$ is a tilt angle between the (hkl) -atomic planes in the substrate and in the layer, arising due to the respective differences in lattice parameters. To describe the strain state of the layer we need to know $\Delta\theta$ and $\Delta\phi$ values

separately. A corresponding routine, based on diffraction measurements with symmetric and asymmetric reflections, is well established for cubic crystals²¹ and allows us to deduce the lattice parameter differences between the layer and the substrate, along, $(\Delta a/a)_{\parallel}$, and perpendicular, $(\Delta a/a)_{\perp}$, to the layer/substrate interface from measured $\Delta\theta$ and $\Delta\phi$ values. For noncubic crystals, the corresponding relationship should be found in accordance with the specific crystal symmetry and orientation. In the next section these relations will be developed for the Y -cut LiNbO₃ under a method that can also be used in a general case.

B. Strain components in Y -cut LiNbO₃: diffraction profile analysis

As was mentioned in Sec. II, comprehensive strain analysis is based on the tensor ξ_{ij} , which in the case of Y -cut LiNbO₃ is given by

$$\xi_{ij} = \begin{bmatrix} \xi_{xx} & 0 & 0 \\ 0 & \xi_{yy} & 0 \\ 0 & 2\varepsilon_{yz} & \xi_{zz} \end{bmatrix}. \quad (23)$$

Tensor ξ_{ij} has this form in Cartesian coordinate system (X, Y, Z) depicted in Fig. 1. However, the measured angular values, $\Delta\theta$ and $\Delta\phi$, are related to the axial strain and the shear strain, respectively, in another coordinate system, viz, in which the atomic planes (hkl) are indexed. Therefore, to express the axial and shear strain components via the components of the deformation tensor ξ_{ij} , some rotation of the tensor ξ_{ij} to the new coordinate system should be performed. Below, a corresponding procedure is introduced for reflections of a type of $(hk0)$ and $(0kl)$, which were used in this research.

For the $(hk0)$ reflection a rotation of the deformation tensor ξ_{ij} should be made around the Z axis, in order to express it in a new coordinate system (X', Y', Z') in which the Y' axis is perpendicular to the reflecting planes and the X' axis is parallel to them. In this coordinate system $\Delta d/d_{(hk0)}$ is equal to ξ'_{yy} , and $\Delta\phi_{(hk0)}$ is equal to ξ'_{yx} . Using standard rotation transformation for the second-rank tensor,¹⁵ the following expressions can be derived:

$$\left(\frac{\Delta d}{d}\right)_{(hk0)} = \sin^2\phi \xi_{xx} + \cos^2\phi \xi_{yy} \quad (24)$$

$$\Delta\phi_{(hk0)} = \sin\phi \cos\phi \cdot (\xi_{yx} - \xi_{xx}),$$

where ϕ is an angle between the reflecting plane $(hk0)$ and the interface.

A similar procedure should be performed for $(0kl)$ reflection, but this time the rotation is around the X axis, thus, the Y' axis is perpendicular to the reflecting plane $(0kl)$ and the Z' axis is parallel to it. In this coordinate system the expressions for $\Delta d/d_{(0kl)}$ and $\Delta\phi_{(0kl)}$ are

$$\left(\frac{\Delta d}{d}\right)_{(0kl)} = \xi'_{yy} = \sin^2 \phi \xi_{zz} + \cos^2 \phi \xi_{yy} \pm \sin \phi \cos \phi (2\varepsilon_{yz}), \quad (25)$$

$$\Delta \phi_{(0kl)} = \xi'_{yz} = \sin \phi \cos \phi (\xi_{yy} - \xi_{zz}) \pm \sin^2 \phi (2\varepsilon_{yz}).$$

In Eqs. (25) the sign $[\pm]$ relates to the sign of the index 1 of the chosen reflection $(0kl)$.

Equations (24) and (25) allow us to deduce the components of tensor ξ_{ij} as a function of the measured parameters $\Delta d/d$ and $\Delta \phi$. Since we used the specific asymmetric reflections (220) and (036) in this experiment, one can specify:

$$\xi_{yy} = \left(\frac{\Delta d}{d}\right)_{(220)} + \tan \phi_{(220)} \Delta \phi_{(220)}, \quad (26)$$

$$\xi_{xx} = \left(\frac{\Delta d}{d}\right)_{(220)} - \cot \phi_{(220)} \Delta \phi_{(220)}, \quad (27)$$

$$\xi_{zz} = \left(\frac{\Delta d}{d}\right)_{(036)} - \cot \phi_{(036)} \Delta \phi_{(036)}, \quad (28)$$

$$2\varepsilon_{yz} = \cot \phi_{(036)} \left(\frac{\Delta d}{d}\right)_{(036)} + \Delta \phi_{(036)} - \cot \phi_{(036)} \xi_{yy}. \quad (29)$$

For LiNbO_3 lattice the angles $\phi_{(220)}$ and $\phi_{(036)}$ are equal to 30° and 32.76° , respectively. Note that formal changing of the Miller indices $(0kl) \rightarrow (0k\bar{l})$ leads to changing the sign of $2\varepsilon_{yz}$. However, it does not influence the further analysis of the experimental data, because only the absolute values of $2\varepsilon_{yz}$ make sense.

By using the symmetric (030) reflection it is possible to directly obtain the ξ_{yy} term of the deformation tensor, since it is defined via the out-of-plane (030) d -spacing difference:

$$\xi_{yy} = \left(\frac{\Delta d}{d}\right)_{(030)}. \quad (30)$$

Equation (30) provides a higher precision for particular term ξ_{yy} than a usage of asymmetric reflection (220) and Eq. (26).

However, it is known²⁷ that despite all precautions the diffraction profile measurements are not accurate enough when the subtle modifications of the in-plane lattice parameters are of the main interest. Generally, this is due to the overlapping of the substrate and the layer diffraction peaks measured in the vicinity of asymmetric reflections. The precision of HRXRD is analyzed in more detail in our paper.²⁸ In case of $Y\text{-LiNbO}_3$ we estimated an accuracy of this mode of measurement as 10^{-4} . Due to the limited accuracy an analysis of experimental profiles based on Eqs. (26)–(30) gave small ($\approx 10^{-4}$) but negative in-plane components of tensor ξ_{ij} . This is unreasonable from the physical point of view, since ion implantation, in general, leads to the swelling of the lattice. Reliable experimental data of significantly enhanced precision ($\approx 10^{-5}$) were obtained by means of x-ray mapping in reciprocal space (RSM).

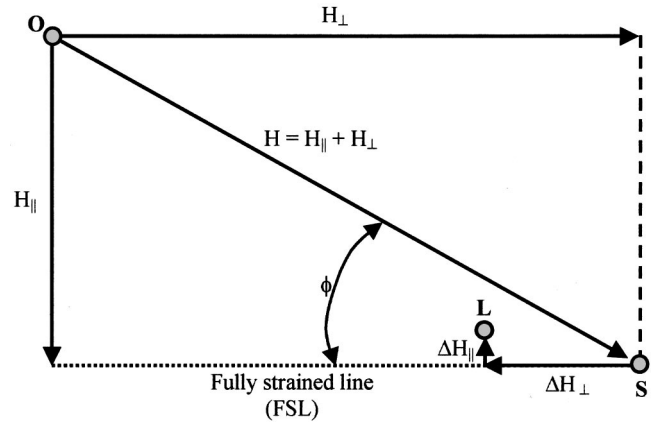


FIG. 5. Schematic drawing of the mapping area in reciprocal space in the vicinity of the node \mathbf{H} . Points of reciprocal lattice, originated in the substrate and in the layer, are indicated by letters \mathbf{S} and \mathbf{L} , respectively.

C. Strain components in the Y -cut LiNbO_3 : X-ray mapping in reciprocal space

RSM measurements were performed with a setup that combined a 18 kW Rigaku rotating anode generator with a Bede D^3 diffractometer. The primary beam ($\text{CuK}\alpha_1$ line) was prepared by two channel-cut (220)Si crystals. The diffracted beam, before entering the detector, passed through the additional channel-cut (220)Si crystal analyzer. In order to afford high-precision measurements of lattice parameter differences between the layers and the substrate, RSM was performed in the vicinity of symmetric (030) LiNbO_3 reflection and two asymmetric LiNbO_3 reflections, (036) and (220).

Details on RSM technique can be found in Refs. 27 and 29 and an analysis of its enhanced precision in Ref. 28. Briefly speaking, in the mapping mode the two-dimensional intensity distribution in the scattering plane is collected by performing $\omega/2\Theta$ scans at different offset ω angles. In the reciprocal space the $\omega/2\Theta$ movement takes place along the vector of reciprocal lattice, \mathbf{H} , while the ω offset is represented in the perpendicular direction (see Fig. 5). Therefore, RSM enables the straightforward separation between the differences in d -spacing (which are revealed on the map along the vector \mathbf{H}), and an angle $\Delta\phi$ between the reflecting planes in the substrate and in the layer (which is revealed along the perpendicular axis).

However, if one is interested in the subtle changes of the in-plane strains a map will be more representative in another coordinate system, viz, with one axis being parallel to the substrate/layer interface (the X or the Z axis in our specific case), and the second one being perpendicular to it (the Y axis for the Y -cut LiNbO_3) (see Fig. 5). In this coordinate system the vector of reciprocal space, $\Delta\mathbf{H}$, which connects the nodes \mathbf{H} of the substrate (\mathbf{S}) and of the layer (\mathbf{L}), is projected to the ΔH_\perp and ΔH_\parallel components. The relationship between the deformation vector \mathbf{u} in real space and the vector $\Delta\mathbf{H}$ in reciprocal space is given by the expression³⁰

$$\Delta\mathbf{H} = -\text{grad}(\mathbf{H} \cdot \mathbf{u}) = -\text{grad}(H_\perp u_\perp + H_\parallel u_\parallel). \quad (31)$$

Substituting Eq. (2) into Eq. (31) yields

$$\Delta H_{\parallel} = -\xi_{\perp,\parallel} H_{\perp} - \xi_{\parallel,\parallel} H_{\parallel} \quad (32)$$

$$\Delta H_{\perp} = -\xi_{\perp,\perp} H_{\perp} - \xi_{\parallel,\perp} H_{\parallel}. \quad (33)$$

If a symmetric reflection is used for RSM measurements, the reciprocal lattice vector \mathbf{H} has no components parallel to the interface ($H_{\parallel} = 0$). Hence, determination of the ΔH_{\perp} and ΔH_{\parallel} magnitudes from the RSM directly yields the $\xi_{\perp,\parallel}$ and $\xi_{\perp,\perp}$ values [the first terms in Eqs. (32) and (33)].

For asymmetric reflections the reciprocal lattice vector \mathbf{H} has both components H_{\perp} and H_{\parallel} . Therefore, both terms in Eqs. (32) and (33) will contribute to the measurable $\Delta \mathbf{H}$ value taken from the map. Hence, RSM in the vicinity of symmetric and asymmetric reflections also allows us to determine the $\xi_{\parallel,\parallel}$ and $\xi_{\parallel,\perp}$ components. Using this method, it is possible to determine a complete set of lattice parameter differences, by choosing appropriate x-ray reflections.

An important particular situation arises if the in-plane lattice parameters of the layer and the substrate exactly match each other. Zero-mismatch value or fully strained state of the layer are good examples. In this case $\xi_{\parallel,\parallel} = 0$ and $\xi_{\perp,\parallel} = 0$, i.e., $\Delta H_{\parallel} = 0$. This means, that on a map taken in the vicinity of an asymmetric reflection, the diffraction intensity will be distributed symmetrically around a straight line that connects the reciprocal lattice points \mathbf{S} and \mathbf{L} and is perpendicular to the interface (i.e., parallel to the ΔH_{\perp}). We will call this a ‘‘fully strained line’’: FSL. The angle between the FSL and the reciprocal vector \mathbf{H} for asymmetric reflection used is equal to the angle ϕ between the reflecting planes and the interface.

An example of the maps taken in the vicinity of the (030) symmetric reflection from an as-implanted sample, as well as from the sample implanted and annealed at 250 °C, is shown in Fig. 6. For an as-implanted sample [Fig. 6(a)] the intensity distribution is concentrated along the line that is parallel to ΔH_{\perp} , because the reciprocal vector $\mathbf{H}_{(030)}$ has no projection onto the interface plane. Equations (32) and (33) are converted to $\Delta H_{\perp} = -\xi_{yy} H_{(030)}$, providing $\xi_{yy} = 7.3 \times 10^{-3}$ for HD layer and $\xi_{yy} = 3.7 \times 10^{-3}$ for LD layer. Annealing at 250 °C results in some additional diffraction intensity along ΔH_{\parallel} [Fig. 6(b)], due to diffuse scattering induced by point defects and their aggregates.¹⁴ Fortunately, the diffuse scattering affects mostly the tails of diffraction profiles and, practically, it does not reduce the accuracy of RSM. However, Fig. 6(b) also shows that the diffraction peaks become blurred along ΔH_{\perp} . Previous research¹⁴ has shown that in samples annealed at elevated temperatures (>200 °C) the out-of-plane component ξ_{yy} varies much more gradually with the crystal depth than in the as-implanted samples. In this situation, the implanted region can hardly be separated into the HD and LD sublayers with certain lattice parameters.

RSM’s taken from an as-implanted sample in the vicinity of the asymmetric (036) and (220) reflections are shown in Fig. 7. It is clearly visible that for both reflections the diffracted intensity is concentrated around straight line with a slope that corresponds exactly to FSL. The intensity distribution is very narrow (close to the theoretically predicted

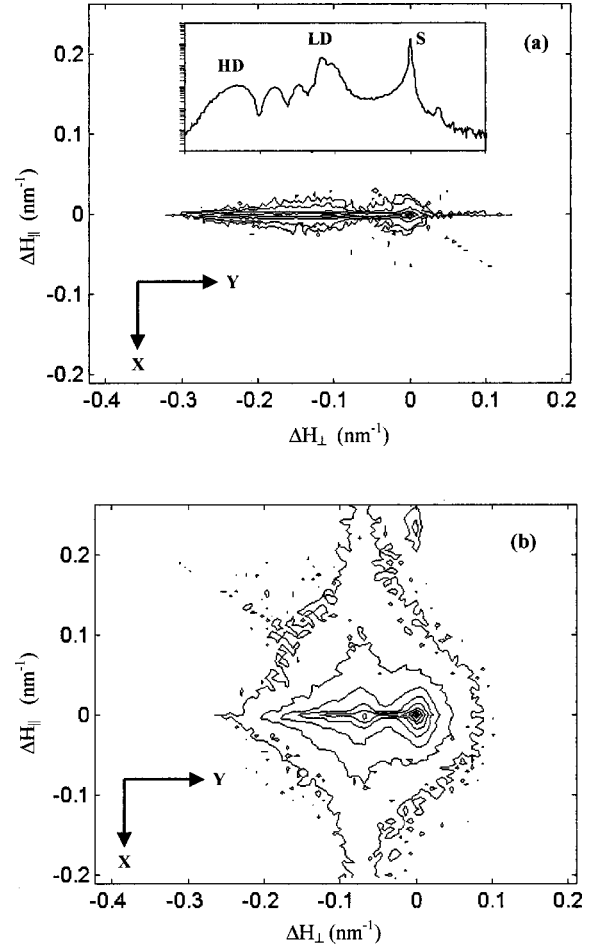


FIG. 6. Reciprocal space maps [symmetric (030) reflection] taken from LiNbO₃ samples: (a) as-implanted; (b) implanted and annealed at 250 °C. Inset in panel (a) shows rocking curve (one-dimensional map cross-section at $\Delta H_{\parallel} = 0$) with peaks from the substrate (S), high-damaged (HD), and low-damaged (LD) regions.

width²⁸) along directions situated in the interface plane, i.e., the Z and X directions, respectively. As a result, the deformation tensor components, ξ_{xx} and ξ_{zz} , were found to be $\xi_{xx} = \xi_{zz} = 0$ with a precision of 2×10^{-5} .

Strain relaxation due to heat treatments is illustrated in Fig. 8, which shows the RSM taken in the vicinity of the asymmetric (220) reflection from the sample implanted and annealed at 250 °C. It can be seen that despite the broadening of the distribution of diffraction intensity along the Y axis (perpendicular to interface), the distribution width along the X and the Z directions (situated in the interface plane) remains very narrow. Due to this circumstance we were able to determine the ξ_{xx} and ξ_{zz} values with the same precision as in an as-implanted sample.

The zoomed image [Fig. 8(b)] demonstrates that the entire intensity distribution is concentrated along the line that is slightly shifted from the FSL by a vector ΔH_x . By measuring these shifts in reciprocal lattice regions that correspond to HD and LD layers, the values of $\xi_{xx} = 8 \times 10^{-5} \pm 2 \times 10^{-5}$ and $\xi_{xx} = 6 \times 10^{-5} \pm 2 \times 10^{-5}$, respectively, were deduced.

A complete set of the precisely determined ξ_{ij} compo-

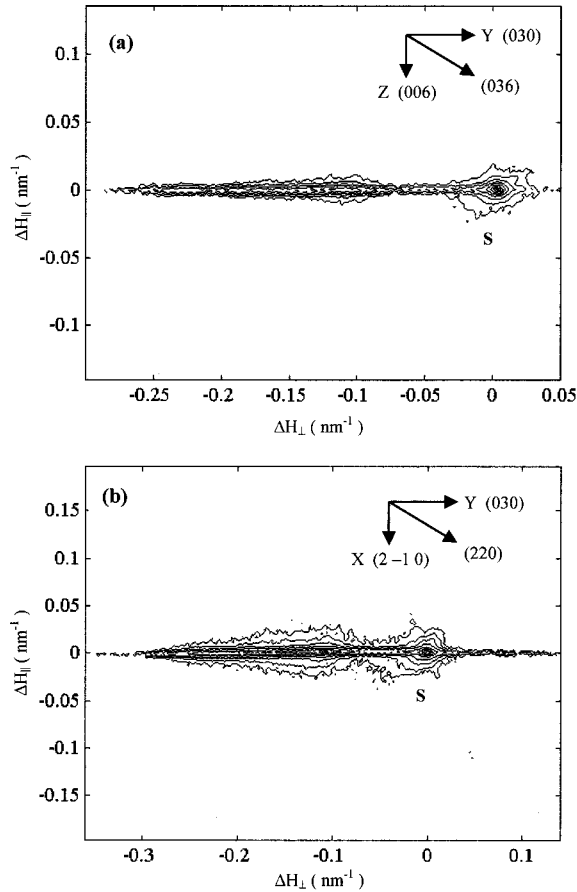


FIG. 7. Reciprocal space maps taken from an as-implanted sample in the vicinity of asymmetric reflections: (a) (036); (b) (220).

nents is given in Table II. Due to enhanced precision, the results obtained by RSM can serve as a reliable database for strain analysis, utilizing equations developed in Sec. II.

IV. DISCUSSION

A. Strain state of implanted and annealed Y-LiNbO₃

As mentioned in Sec. II, the assumption, $m_{yy} = m_{xx}$, which implies that the unit cell of implanted LiNbO₃ keeps its initial rhombohedral symmetry, provides a unique solution for lattice mismatches and strain degrees [see Eq. (20)]. However, this equality cannot be asserted in advance, but should be checked by using Eq. (21). The differences, $A = m_{yy} - m_{xx}$, calculated by means of the measured ξ_{ij} values are also given in Table II.

Table II provides direct evidence that in all measured samples the A values are positive and much larger than the measurements errors ($\approx 10^{-5}$). For example, $A = 6 \times 10^{-3}$ was determined in the HD layer of an as-implanted sample. Therefore, it can be concluded that the swelling along the Y direction in an implanted layer (in its hypothetical free-standing state) is much larger than that along the X direction. This means that the initial rhombohedral symmetry is broken due to the implantation processing. If we follow a rule that the reduced symmetry should be described by a subgroup of

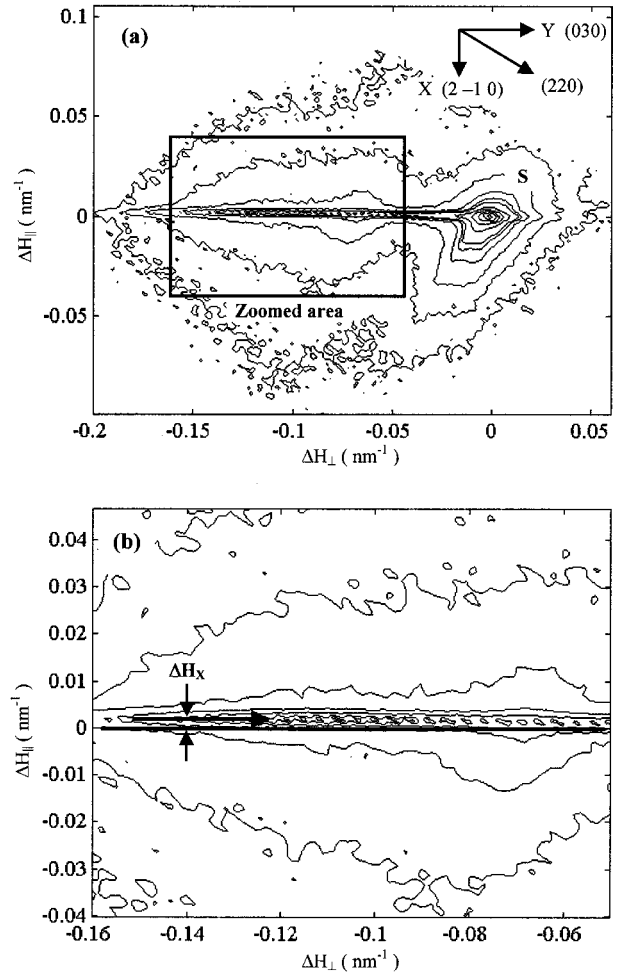


FIG. 8. Reciprocal space map in the vicinity of the asymmetric (220) reflection taken from the sample, implanted and annealed at 250 °C. (a) Entire mapping area; (b) Enlargement of the layer's peak region.

the initial point group $3m$, the modified unit cell presumably belongs to the monoclinic symmetry. This conclusion stems from the following considerations: the breakdown of the rhombohedral symmetry implies that the three-fold axis definitely disappears as a result of ion implantation; the remaining second symmetry element, the mirror plane, may be found as the unique symmetry element only in the monoclinic system, viz, in the point group m . This result can be made more visual in the hexagonal setting of the initial unit cell. Implantation-induced symmetry reduction to monoclinic can be driven by small deviations from the initial angle, $\alpha = 120^\circ$, between corresponding translation vectors. Simple geometric considerations yield the deviation angle, $\Delta\alpha$, linearly proportional to A value, viz, $\Delta\alpha = 2A\sqrt{3}$. The latter expression, for example, provides $\Delta\alpha = 1.2^\circ$ for the HD layer of an as-implanted sample. Post-implantation annealing results in the partial lattice recovery toward the initial rhombohedral symmetry and, correspondingly, to a decrease of the deviation angle $\Delta\alpha$ (see Table II).

Anisotropy of lattice mismatch can be explained in terms of strain-induced ordering of point defects, which reduces

TABLE II. Summary of the RSM results.

Sample	Layer	$\xi_{xx} (\times 10^4)$	$\xi_{yy} (\times 10^4)$	$\xi_{zz} (\times 10^4)$	$2\varepsilon_{yz} (\times 10^4)$	$A (\times 10^4)$	$\Delta\alpha$ (deg)
As impl.	HD	0	73	0	3.8	60	1.2
	LD	0	37	0	1.9	30	0.6
Annealed 200 °C	HD	<0.2	56	<0.2	2.4	48	0.95
	LD	0.4	20	<0.2	1.2	15	0.3
Annealed 250 °C	HD	0.8	26	0.4	1	22	0.44
	LD	0.6	16	0.4	0.6	13	0.25
Annealed 350 °C	LD	<0.2	9.6	<0.2	<0.4	8	0.15

the strain energy of the system by decreasing the in-plane mismatch. Such ordering is a well-known phenomenon in the field of physical metallurgy,³¹⁻³⁴ and interstitial carbon in bcc iron is an example. However, to the best of our knowledge such ordering has not been observed in single crystals used for modern microelectronics and optoelectronics.

Strain-induced defect ordering can take place if defects introduce a local strain field having a symmetry lower than that of the initial lattice, i.e., they cause a local anisotropic deformation of the crystal. An ordering mechanism of such defects is schematically illustrated in Fig. 9.

During an ordering process the point defects jump to the neighboring sites, and the new defect states can be described in terms of orientation changing due to the anisotropy mentioned. The characteristic time of this jumping is much shorter as compared to other creep mechanisms, which cause a plastic deformation due to dislocation gliding or the long-range diffusion.

For further analysis, it is worthwhile to recall Sec. II in order to include the strain-induced ordering in the general elasticity problem. It will be helpful to split the lattice mismatch tensor m_{ij} given by Eq. (1) into two terms:

$$m_{ij} = f_{ij} + g_{ij}. \quad (34)$$

The first tensor f_{ij} reflects the symmetry of the initial unit cell and describes a hypothetical situation of lattice modification, with no elastic strains and ordering effects. The components of tensor f_{ij} linearly follow the atomic concentration in case of epitaxially grown layers (via Vegard rule), or the point-defect concentration in case of an implanted crystal.

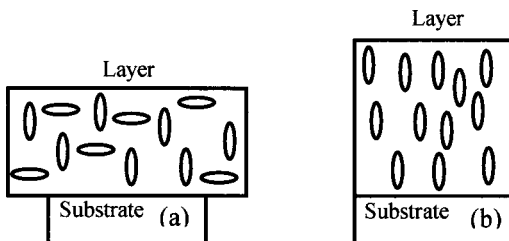


FIG. 9. Schematic illustration of point-defect influence on the lattice mismatch: (a) Random defect distribution, (b) Defect ordering along the direction of preferred orientation.

The second tensor g_{ij} describes anisotropic deformation caused by strain-induced ordering. In case of implanted Y -cut LiNbO_3 ,

$$f_{ij} = \begin{bmatrix} \frac{m_{xx} + m_{yy}}{2} & 0 & 0 \\ 0 & \frac{m_{xx} + m_{yy}}{2} & 0 \\ 0 & 0 & m_{zz} \end{bmatrix}, \quad (35)$$

$$g_{ij} = \begin{bmatrix} -\frac{m_{yy} - m_{xx}}{2} & 0 & 0 \\ 0 & \frac{m_{yy} - m_{xx}}{2} & 0 \\ 0 & 0 & 0 \end{bmatrix}. \quad (36)$$

A degree of lattice mismatch anisotropy can be described by a parameter $0 \leq p \leq 1$:

$$p = \frac{m_{yy} - m_{xx}}{m_{yy} + m_{xx}}, \quad (37)$$

which gives the ratio between the deformation caused by strain-induced ordering and the isotropic lattice swelling in the X - Y plane. The value $p=1$ relates to the fully anisotropic unit cell ($m_{xx}=0$), while $p=0$ describes the fully isotropic state with $m_{xx}=m_{yy}$.

Although the mismatch components and strain degrees in our samples cannot be found in terms of the unique solution of Eq. (20), it is possible to pinpoint the intervals of parameters that fit experimental data. These intervals can be expressed via a single variable p by substituting its definition (37) into Eq. (20):

$$m_{xx} = \frac{A}{2} \left(\frac{1}{p} - 1 \right), \quad (38)$$

$$m_{yy} = \frac{A}{2} \left(\frac{1}{p} + 1 \right),$$

$$m_{zz} = \xi_{zz} + \frac{1}{0.372} \left[\xi_{yy} + 0.279\xi_{xx} - \frac{A}{2} \left(1.279 \frac{1}{p} + 0.721 \right) \right],$$

$$S_x = 1 - \xi_{xx} \frac{2p}{A(1-p)},$$

$$S_z = 1 - \frac{\xi_{zz}}{\xi_{zz} + \frac{1}{0.372} \left[\xi_{yy} + 0.279\xi_{xx} - \frac{A}{2} \left(1.279 \frac{1}{p} + 0.721 \right) \right]}.$$

According to Eqs. (12) and (13), the following conditions must be fulfilled:

$$m_{xx} \geq \xi_{xx} \quad \text{and} \quad m_{zz} \geq \xi_{zz}. \quad (39)$$

Substituting m_{xx} and m_{zz} from Eq. (38) into Eq. (39) yields an interval of possible values for the anisotropy parameter p :

$$\frac{A}{\xi_{yy} + \xi_{xx} + 1.947(2\varepsilon_{yz})} \leq p \leq \frac{A}{A + 2\xi_{xx}}. \quad (40)$$

Equation (40) together with the numerical data from Table II leads to the conclusion that in all waveguide layers the anisotropy degree $p > 0.7$. According to the definition (37), this means that the implantation-induced mismatch along the Y direction is at least six times larger than that along the X direction. In samples annealed at 200 and 250 °C, a similar analysis also revealed an upper limit for the anisotropy degree, $p < 0.93$, which stems from the fact that $\xi_{xx} \neq 0$.

By substituting the measured data from Table II in Eq. (38), the permitted values of the mismatch components can be represented as a function of the parameter p . Examples of the plots calculated for the HD layer in an as-implanted sample, as well as for the LD layer in sample implanted and annealed at 250 °C, are shown in Fig. 10.

The accomplished strain analysis allowed us to draw an important conclusion, that due to the strain-induced ordering of point defects the in-plane lattice mismatches and related strain components in the waveguide layers are close to zero in the absolute scale. This means that the main contribution to the modification of refractive index comes from the simple implantation-induced lattice swelling, leading to the proportional reductions in the electron density and refraction index, $\Delta n/n \approx \xi_{yy}$. The role of the photoelastic effect is negligible.

B. Relaxation mechanism of the implanted layer

Strained heterostructures may exhibit two types of strain relaxation mechanisms, according to the two terms, which compose the in-plane strain component, $\varepsilon_{ii} = -m_{ii} \pm n_i b_i$. Conventional strain relaxation due to formation of misfit dislocations reduces ε_{ii} at the expense of an increasing dislocation density n_i . The amount of strain reduction by this mechanism is directly related to the in-plane lattice parameter differences ξ_{xx} and ξ_{zz} [see Eq. (9)]. The second mechanism is based on the diminishing of the lattice mismatch m_{ii} as a result of the atomic rearrangements. In grown heterostructures the rearrangement mentioned can, in principle, be

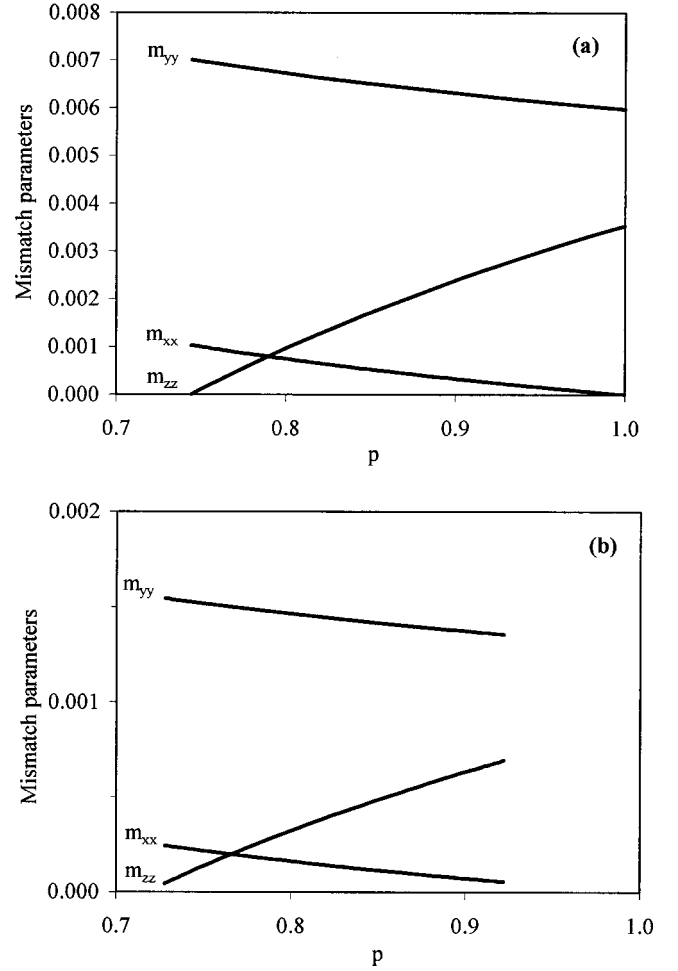


FIG. 10. Mismatch parameters as a function of the anisotropy parameter, p : (a) In the HD layer of an as-implanted sample; (b) In the LD layer of the sample, implanted and annealed at 250 °C.

driven by atomic diffusion,³⁵ although in most practical cases atomic diffusion at room and elevated temperatures is too slow to be taken into account. Results presented here show that in systems in which the lattice mismatch is produced by point defects, this rearrangement can be very important. Annealing of point defects reduces the strain energy via diminishing the mismatch components [the first term in Eq. (10)]. As was pointed out in Ref. 14, annealing at temperatures higher than 200 °C leads to the fast lattice recovery and considerable reduction in the optical barrier $B = \xi_{yy}$ in the waveguide layer.

In this research we have carried out additional temperature measurements of the $B(T)$ values in order to follow kinetics of lattice recovery in more detail. For this purpose the (030)LiNbO₃ diffraction profiles were taken from implanted and isochronously (for $t_0 = 30$ min) annealed samples at temperatures ranging between 225 and 470 °C. The depth-dependent ξ_{yy} profiles similar to those plotted in Fig. 3 were obtained as a result of fittings, using dynamical diffraction theory (see, e.g., Refs. 22 and 23). Reduction of the optical barrier $B(T)$ with temperature was treated in terms of Debye relaxation model:

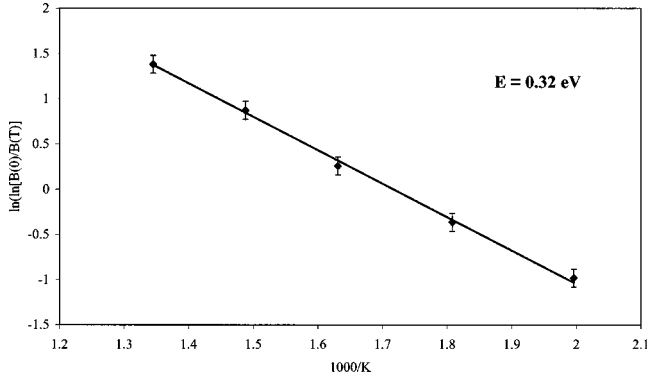


FIG. 11. Arrhenius plot, showing the temperature-dependent diminishing of the implantation-induced lattice swelling along the Y axis.

$$B(T) = B(0) \exp\left(-\frac{t_0}{\tau}\right) \quad (41)$$

with the relaxation time τ defined by an activation energy ΔE :

$$\tau = \tau_0 \exp(\Delta E/kT). \quad (42)$$

Using Eqs. (41) and (42), we can present the temperature behavior of the optical barrier $B(T)$ in the Arrhenius-like form:

$$\ln\left[\ln\frac{B(0)}{B(T)}\right] = \ln\frac{t_0}{\tau_0} - \frac{\Delta E}{kT}. \quad (43)$$

Experimental data plotted in this format are well fitted by straight line (see Fig. 11), providing an activation energy of $\Delta E = 0.32$ eV, which coincides with the one obtained previously.¹⁴ This ΔE value is much less than the characteristic energies required for dislocation formation, and this gives some additional proof that, in our case, the situation is completely controlled by point defects.

V. SUMMARY

Heterostructures of reduced crystal symmetry (especially belonging to the hexagonal and rhombohedral systems) attract great deal of attention in structural studies due to a growing interest to use them in modern microelectronic and optoelectronic noncubic crystalline systems. For this purpose a general approach to solving the elasticity problem is formulated, which does not rely on the isotropy assumption for lattice mismatch or misfit dislocations density. The developed routine permits us, in principle, to obtain complete information on all strain-tensor components.

Calculation steps are described with a focus on the Y -cut LiNbO_3 . As a result, a set of equations is derived, which connect the measured modifications of lattice parameters and the intrinsic structural characteristics, such as lattice mismatches and strain degrees. In general, these equations enable us to check the validity of the Vegard rule and/or to reveal the strain-induced breakdown of the initial unit cell symmetry. As a consequence of avoiding any prelimi-

nary assumptions, an extra degree of freedom appears in the equation set, which results in an interval of parameters matching the experimental data, rather than the unique solution.

This approach, being applied to the rhombohedral LiNbO_3 , allows us to shed some additional light on structural modifications evolving in the near-surface waveguide layers as a result of ion implantation and subsequent annealing. Using RSM in the vicinity of symmetric and asymmetric reflections, we were able to precisely measure lattice parameter changes with an accuracy of $\Delta a/a \approx 10^{-5}$ and thus to obtain comprehensive information on the in-plane and out-of-plane strain components, including shear strains.

Experimental results show that the He-implantation causes significant modification of the out-of-plane lattice parameter, while the in-plane lattice parameters remain matched to those of a crystal bulk, which means that implanted layers are fully strained. However, in an absolute scale the in-plane strain components were found to be close to zero. Heat treatments lead to the rapid relief of the out-of-plane lattice parameter while only subtle modifications of the in-plane lattice parameters, $\Delta d/d_{\parallel} < 8 \times 10^{-5}$, were detected using sensitive RSM technique.

It was found that the lattice mismatch in the X direction of the initial rhombohedral unit cell is significantly smaller (by at least a factor of 6) than that in the Y direction. This is the first direct observation of the implantation-induced anisotropy of lattice mismatch which, from the symmetry point of view, is expected to be isotropic in the XY -plane. The obtained results indicate a reduction in the initial rhombohedral symmetry, presumably to the monoclinic one. This effect is explained in terms of the strain-induced ordering of point defects, which reduces certain strain components acting in the interface plane and, correspondingly, the total strain energy of the system. Taking this effect into account, it is possible to conclude that modifications of the refractive index in an implanted LiNbO_3 are mainly due to the implantation-induced lattice swelling in the Y direction (and related reduction of electron density) rather than due to the optoelastic effect.

Strain-induced ordering of point defects is a well-established phenomenon in the field of physical metallurgy, but to the best of our knowledge has been never mentioned in the studies of thin film heterostructures. Because of its potential importance to other layered structures, this phenomenon was included in the general formulation of the elasticity problem for layered crystalline structures.

ACKNOWLEDGMENTS

We thank the Implantation group of the Technion, and especially Dr. V. Richter, for supplying us with implanted samples. The Wolfson Center for Interface Studies at the Technion is gratefully acknowledged for free access to the x-ray facility.

- ¹ *Semiconductors and Semimetals*, edited by R. K. Willardson and A. C. Beer (Academic, New York, 1990), Vol. 32.
- ² J. Hornstra and W. J. Bartels, *J. Cryst. Growth* **44**, 513 (1978).
- ³ E. Anastassakis, *J. Appl. Phys.* **68**, 4561 (1990).
- ⁴ K. Yang, T. Anan, and L. J. Schowalter, *Appl. Phys. Lett.* **65**, 2789 (1994).
- ⁵ H. Heinke, A. Waag, M. O. Moller, D. Hommel, and G. Landwehr, *J. Cryst. Growth* **135**, 41 (1994).
- ⁶ C. Giannini, L. Tapfer, T. Peluso, N. Lovergine, and L. Vasanelli, *J. Phys. D* **28**, A125 (1995).
- ⁷ K. L. Kavanagh, M. A. Capano, L. W. Hobbs, J. C. Barbour, P. M. J. Maree, W. Schaff, J. W. Mayer, D. Pettit, J. M. Woodall, J. A. Stroschio, and R. M. Fenstra, *J. Appl. Phys.* **64**, 4843 (1988).
- ⁸ B. K. Tanner, A. G. Turnbull, C. R. Stanley, A. H. Kean, and M. McElhinney, *Appl. Phys. Lett.* **59**, 2272 (1991).
- ⁹ M. Schuster, P. O. Gervais, B. Jobst, W. Hosler, R. Averbeck, H. Riechert, and A. Iberl, *J. Phys. D* **32**, A56 (1999).
- ¹⁰ E. Berkowicz, D. Gershoni, G. Bahir, E. Lakin, D. Shilo, E. Zolotoyabko, A. C. Abare, S. P. Denbaars, and L. A. Coldren, *Phys. Rev. B* **61**, 10 994 (2000).
- ¹¹ D. J. Bottomley, P. Fons, and D. J. Tweet, *J. Cryst. Growth* **154**, 401 (1995).
- ¹² P. D. Townsend, *Rep. Prog. Phys.* **50**, 501 (1987).
- ¹³ L. Zhang, P. J. Chandler, and P. D. Townsend, *Nucl. Instrum. Methods Phys. Res. B* **59/60**, 1147 (1991).
- ¹⁴ Y. Avrahami and E. Zolotoyabko, *Nucl. Instrum. Methods Phys. Res. B* **120**, 84 (1996).
- ¹⁵ J. F. Nye, *Physical Properties of Crystals* (Clarendon Press, Oxford, 1985).
- ¹⁶ J. W. Matthews, in *Epitaxial Growth*, edited by J. W. Matthews (Academic, New York, 1975), Pt. B.
- ¹⁷ M. Levy, H. Bass, and R. Stern, *Hand-Book of Elastic Properties of Solids Liquids and Gases* (Academic, New York, 2000), Vol. 1.
- ¹⁸ S. N. G. Chu, A. T. Macrander, K. E. Strege, and W. D. Johnston, *J. Appl. Phys.* **57**, 249 (1985).
- ¹⁹ E. Zolotoyabko, A. Goldner, and Y. Komem, *Phys. Rev. B* **60**, 11 014 (1999).
- ²⁰ R. S. Weise and T. K. Gaylord, *Appl. Phys. A: Mater. Sci. Process.* **37**, 191 (1985).
- ²¹ W. J. Bartels and W. Nijman, *J. Cryst. Growth* **44**, 518 (1978).
- ²² W. J. Bartels, J. Hornstra and D. J. W. Lobeek, *Acta Crystallogr., Sect. A: Found. Crystallogr.* **42**, 539 (1986).
- ²³ P. F. Fewster, *Semicond. Sci. Technol.* **8**, 1915 (1993).
- ²⁴ E. Zolotoyabko, *J. Appl. Crystallogr.* **31**, 241 (1998).
- ²⁵ C. Glorieux and E. Zolotoyabko, *J. Appl. Crystallogr.* (to be published).
- ²⁶ Y. Avrahami and E. Zolotoyabko, *J. Appl. Phys.* **85**, 6447 (1999).
- ²⁷ D. K. Bowen and B. K. Tanner, *High Resolution X-Ray Diffraction and Topography* (Taylor & Francis, London, 1998).
- ²⁸ D. Shilo, E. Lakin, and E. Zolotoyabko, *J. Appl. Crystallogr.* (to be published).
- ²⁹ P. F. Fewster, *Crit. Rev. Solid State Mater. Sci.* **22**, 69 (1997).
- ³⁰ S. Takagi, *Acta Crystallogr.* **15**, 1311 (1962).
- ³¹ A. S. Nowick and B. S. Berry, *Anelastic Relaxation in Crystalline Solids* (Academic, New York, 1972).
- ³² A. S. Nowick and B. S. Berry, in *Physical Acoustics*, edited by W. P. Mason (Academic, New York, 1966), Vol. 3, Pt. A.
- ³³ C. Wert, in *Physical Acoustics* (Ref. 32).
- ³⁴ C. Zener, *Elasticity and Anelasticity of Metals* (The University of Chicago Press, Chicago, 1948).
- ³⁵ N. Cowern, P. C. Zalm, P. van der Sluis, D. J. Gravesteyn, and W. B. de Boer, *Phys. Rev. Lett.* **72**, 2585 (1994).